

# Fundamental SNR Limits imposed by ASE in Frequency-Shifting Loops

Carlos R. Fernández-Pousa, *Senior Member, OSA, IEEE*, and Hugues Guillet de Chatellus

**Abstract**—Recirculating frequency-shifting loops (FSLs) are a simple source of optical frequency combs with bandwidth compatible with microwave technologies. As such, they have demonstrated promising capabilities for telecommunications, remote sensing, and microwave photonics. In these systems, the coherent frequency comb is produced by recirculation of a single frequency laser in a fiber loop containing a frequency shifter. Due to the insertion of an optical amplifier in the loop to compensate for the losses, amplified spontaneous emission (ASE) is inevitably emitted and superimposes to the coherent output. In this paper, we quantify theoretically the contribution of the ASE background to the FSL output for different types of receivers used in FSL-based techniques: direct, self-heterodyne, and dual-comb detection. In particular, we focus on two important practical applications of FSL: coherent optical reflectometry and real-time Fourier transforms of radio-frequency signals. We provide for each of them numerical estimations of the signal-to-noise ratio and dynamic range. This work constitutes a compact framework for the general evaluation of techniques based on FSLs.

**Index Terms**—Frequency shifting loops, ASE noise, microwave photonics, optical frequency comb, signal to noise ratio.

## I. INTRODUCTION

The growing need for reliable sensing and signal processing techniques at large has triggered the occurrence of numerous novel techniques based on photonics over the last 20 years. Combining low power consumption, immunity to electromagnetic interference, directivity, large bandwidth, availability of low-cost telecom components and potential integration, photonics offers many advantages as compared to conventional sensing or signal processing techniques based on microwaves (MW). In particular, photonics has proven a reliable platform both for metrology, including remote sensing and Lidar [1], [2], and for microwave photonics, namely the generation, the transport, and the processing of MW signals based on photonics [3], [4]. The advent of photonic techniques to practical real-world applications was facilitated by the availability of compact coherent light sources at the telecom wavelength, including narrow-linewidth lasers and frequency combs, and of broadband modulators and detectors enabling an easy conversion between the MW and the optical domain.

C. R. Fernández-Pousa is with the Engineering Research Institute (I3E) and the Department of Communications Engineering, Universidad Miguel Hernández, 03202 Elche, Spain (e-mail: c.pousa@umh.es).

Hugues Guillet de Chatellus is with the LIPhy, UGA/CNRS, 38000 Grenoble, France (e-mail: hugues.guilletdechatellus@univ-grenoble-alpes.fr).

Manuscript submitted Feb. 8, 2022. This work was supported in part by Ministerio de Ciencia e Innovación and Agencia Estatal de Investigación (MCIN/AEI/10.13039/501100011033) under Grant PID2020-120404GB-I00, and also in part by the Agence Nationale de la Recherche and Direction Générale de l'Armement under Grant ANR 16-ASTR-015. (*Corresponding author: Carlos R. Fernández-Pousa.*)

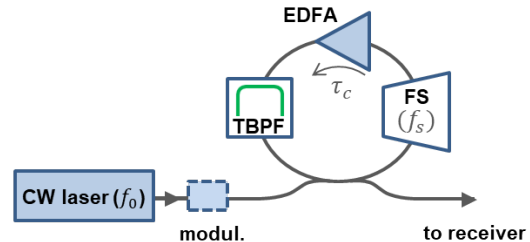


Fig. 1. Generic sketch of a frequency shifting loop (FSL) injected by a CW laser (frequency:  $f_0$ ). The loop contains an amplifier (EDFA), an optical tunable bandpass filter (TBPB), and a frequency shifter (FS). A modulator can be inserted on the injection arm. The FSL roundtrip time and the frequency shift per roundtrip are respectively denoted by  $\tau_c$  and  $f_s$ .

In this context of intense technological development, an original photonic architecture, so-called recirculating frequency-shifting loops (or FSLs), has proven a powerful, yet simple tool for multiple applications in telecommunications, sensing and signal processing.

Essentially, FSLs are based on a cavity, or a fiber loop, incorporating a frequency shifter (Fig. 1). The latter can be based on acousto-optic or on electro-optic interaction. A coupler enables to seed the FSL and to extract a fraction of the optical signal circulating in the loop. When seeded with a single frequency laser (frequency:  $f_0$ ), the recirculation of the optical field in the loop gives birth to an optical frequency comb, i.e. a set of equidistant spectral lines starting at the frequency of the seed laser and spaced by the frequency shift ( $f_s$ ) [5]–[9]. To compensate for the unavoidable losses of the loop, an amplifier is generally inserted, as well as an optical bandpass filter. The role of the filter is double: to control the number of lines of the comb, and to limit the amplified spontaneous emission (ASE) produced by the optical amplifier. In practice, the effects of gain saturation and the role played by ASE tend to limit the maximum number of comb lines to a few hundreds. In the case of electro-optic frequency shifters based on single sideband Mach-Zehnder interferometers, the frequency shift is usually in the GHz range [5], enabling multiplexed optical networks in telecommunications [6], [7], [10], [11]. In the case of an acousto-optic frequency shifter operating at a few tens of MHz, the total resulting comb bandwidth amounts to a few tens of GHz, a value notably smaller than mode-locked optical frequency combs, whose bandwidth extends over several nanometers. However, acousto-optic FSLs, which only involve slow electronics (tens of MHz), have a different scope. They have turned out to be an efficient platform enabling the generation and the processing of waveforms with

bandwidth in the tens of GHz range and compatible with standard MW technologies. As such, FSLs seeded with a CW laser have shown applications in coherent optical reflectometry [12], remote sensing [13], multi-heterodyne spectroscopy [14], or generation of light pulses with multi GHz repetition rates [15], [16].

When the seed laser is modulated before its injection in the loop by a radio-frequency (RF) signal, the FSL generates a large set of replicas of this input signal, shifted both along the temporal, and the frequency domain. More precisely, defining  $\tau_c$  as the roundtrip time of the light in the FSL, the replica labelled by the integer  $n$  has been temporally delayed by  $n\tau_c$  and frequency shifted by  $nf_s$ . The FSL output results in a coherent superposition to these replicas, a property at the heart of practical demonstrations of analog RF signal processing, such as real-time Fourier and fractional Fourier analysis by frequency to time mapping [17], [18], signal filtering [19], [20], ultrafast signal characterization [21], and arbitrary waveform generation [22].

The FSL can also be injected with a pulse whose width is lower than the roundtrip time  $\tau_c$ . In this case, the FSL acts as a frequency translation circuit that outputs a series of pulses carried by a progressive frequency, equal in number to the number or recirculations. This type of systems finds applications, for instance, in heterodyne Brillouin OTDR [23] and as photonic generators for stepped-frequency radars [24].

Beside the spectral bandwidth and the domains of application, acousto-optic frequency combs show another significant difference with mode-locked optical frequency combs. In these, the cavity plays an important role on the output spectrum by filtering out ASE between the lines. In FSLs, due to the presence of the frequency shifter, the cavity does not provide spectral filtering in the usual sense. Any spontaneous photon emitted by the amplifier will travel in the FSL whatever its frequency [25]. Therefore, ASE plays a stronger role in FSLs than in classical mode-locked optical frequency combs. For instance it has been shown that in standard experimental situations, the total power of ASE at the FSL output can be comparable to, or even exceed the total power of the comb [26]. Therefore, the role of ASE in the output signal cannot be neglected. So far, the research devoted to the influence of ASE noise in FSLs has limited to an analysis in the spectral domain and in the permanent regime [26], [27] or in frequency translation circuits [28]–[30]. To our knowledge, no research work has been devoted to the role of ASE noise on the output temporal signal. Still, ASE noise directly sets the limits of the system. To give an example, the ASE background constraints the dynamics of spectral analysis in FSLs. Moreover, it also reduces the signal-to-noise ratio of ranging experiments based on FSL.

The objective of this paper is to provide an extensive theoretical analysis of the effect of ASE on the signal received at the FSL output, to help assess the practical utility of FSL-based applications, and develop means to optimize them. Though our strategy of analysis is valid for both electro-optic and acousto-optic FSL, the numerical estimates of the SNR and the application examples will be based on the latter systems. The paper is structured as follows. First, we characterize

the electric field at the FSL output as the superposition of the coherent signal and of the recirculating ASE noise. Then we derive analytically the expression of the signal-to-noise ratio (SNR) and of the dynamic range (DR) at the FSL output for various receivers and detection schemes. More precisely, we consider the three following cases encountered in different applications of FSLs:

- *Direct detection.* The FSL output is directly sent to a broadband photodetector.
- *Self-heterodyne detection.* The FSL output is mixed on a broadband photodetector with a fraction of the seed laser that acts as a local oscillator. This detection scheme enables coherent detection and processing of the FSL output and can be combined with digital correlation.
- *Multi-heterodyne dual-comb correlation detection.* This detection scheme, similar to multi-heterodyne interferometry, consists in mixing on a narrowband photodetector the FSL output with a second optical frequency comb mutually coherent with the first one.

Finally, we illustrate our analysis by focusing on the SNR and the DR in two representative and practical scenarios: coherent optical reflectometry and real-time Fourier transform.

## II. THE FSL FIELD WITH ASE NOISE

As was schematically shown in Fig. 1, recall that a FSL encompasses a gain medium, typically an EDFA, that compensates for the optical losses in the loop, an optical filter that rejects ASE and limits the optical bandwidth of the generated frequency comb, and a frequency shifter. The loop is externally injected by a highly coherent CW laser frequency  $f_0$ , so that the frequencies in the optical comb are  $f_n = f_0 + nf_s$ , with  $n = 0, \dots, N-1$  and  $N$  the total number of lines. We define  $s_0$  as the seed power of the FSL. In the rotating frame at frequency  $f_0$ , the electric field in the permanent regime at the output of the FSL writes [31], [32]:

$$e(t) + \epsilon(t) = \sum_{n=0}^{N-1} \sqrt{s_n} e^{-i\phi_n} e^{i2\pi n f_s (t-\tau)} + \epsilon(t) \quad (1)$$

In this equation,  $e(t)$  is the (noiseless) optical comb,  $\epsilon(t)$  is the recirculating ASE noise produced in the FSL,  $s_n$  is the optical power of the  $n$ -th spectral line,  $\phi_n = \pi f_s \tau_c n^2$  its phase, and  $\tau = \tau_c f_0 / f_s + \tau_c / 2$  is a global delay that depends linearly on the seed frequency  $f_0$ . Note that the ASE noise generated by the EDFA is unpolarized, but the frequency shifter blocks one of its polarizations. Hence, the recirculation process that originates (1) takes place in a single, linear polarization.

The temporal waveforms described by (1) are determined by the comb's spectral phases  $\phi_n$  and can be classified according to the theory of temporal Talbot effect: when the product  $f_s \tau_c$  equals an integer value, a requirement termed integer Talbot condition, the comb describes an optical train of transform-limited pulses at a repetition rate  $f_s$ . When  $f_s \tau_c$  equals a rational number  $p/q$  (fractional Talbot condition), each period  $1/f_s$  of the train contains  $q$  transform-limited pulses whose relative phases are organized following a quadratic law, resulting in a  $q$ -fold increase of the intensity's repetition rate [15], [31], [32]. Finally, when the product  $f_s \tau_c$  departs from integer

or fractional Talbot conditions say, by a small change  $\delta f$  of the shifting frequency, pulses stretch under the action of an effective first-order dispersion  $\tau_c \delta f / f_s^2$  and the train becomes composed of linearly chirped optical pulses [33], [34].

The  $n$ -th spectral line in (1) is generated after  $n$  recirculations of the seed frequency in the loop, undergoing in each round trip a frequency shift  $f_s$ , an EDFA power gain  $G$  and a power loss described by the transmission coefficient of the loop over one round trip,  $T < 1$ . Its power is therefore:

$$s_n = (GT)^n s_0 \quad (2)$$

and the total comb's power is:

$$P_{\text{comb}} = \sum_{n=0}^{N-1} (GT)^n s_0 = s_0 \frac{1 - (GT)^N}{1 - GT} \quad (3)$$

Two limit cases are worth considering: when  $(GT)^N \ll 1$  the comb has a purely decaying shape, the role of the optical filter is solely to reject ASE, and  $P_{\text{comb}} = s_0 / (1 - GT)$ . In turn, when  $GT \rightarrow 1$  the comb has a flat power over a bandwidth determined by the optical filter, and  $P_{\text{comb}} = N s_0$ .

The ASE field  $\epsilon(t)$  can also be decomposed in  $N$  different spectral slices  $\alpha_n(t)$  of width  $f_s$  and centered at  $n f_s$  ( $n = 0, \dots, N-1$ ) according to:

$$\epsilon(t) = \sum_{n=0}^{N-1} \alpha_n(t) e^{i2\pi n f_s t} \quad (4)$$

The spectrum of the baseband fields  $\alpha_n(t)$  is contained in the interval  $[-f_s/2, f_s/2]$  and the total FSL optical bandwidth is thus  $N f_s$ . The ASE power in the  $n$ -th band will be denoted by  $a_n = \langle |\alpha_n(t)|^2 \rangle$ , where the brackets stand for statistical average. As is discussed in Appendix A, the recirculation process induces mutual correlations between the  $\alpha_n(t)$  fields which nonetheless show a simple recurrence in power [26]:

$$a_n = GT \cdot a_{n-1} + a_0 \quad (5)$$

Here,  $a_0$  is the single-pass ASE power generated by the amplifier in a bandwidth  $f_s$  and in one polarization,  $a_0 = n_{sp} h \nu (G-1) f_s$ , where  $n_{sp}$  is the spontaneous emission factor ( $n_{sp} > 1$ ), and  $h$  and  $\nu$  are respectively the Planck's constant and the central frequency of the photons ( $\simeq f_0$ ). With a typical value of the gain  $G = 10$  and using  $f_s = 80$  MHz, also typical for acousto-optic FSL,  $a_0$  is of the order of 0.1 nW. For  $f_s = 8$  GHz (electro-optic FSL),  $a_0$  is close to 10 nW. According to (5), the ASE power grows from slice to slice following the shifting frequency, until the growth is finally cut off by the optical filter. Recurrence (5) is solved as [26]:

$$a_n = a_0 \sum_{k=0}^n (GT)^k = a_0 \frac{1 - (GT)^{n+1}}{1 - GT} \quad (6)$$

and so the spectrum has the staircase structure with steps of width  $f_s$  shown in Fig. 2. The total ASE power becomes:

$$P_{\text{ASE}} = \sum_{n=0}^{N-1} a_n = a_0 \left[ \frac{N}{1 - GT} - GT \frac{1 - (GT)^N}{(1 - GT)^2} \right] \quad (7)$$

which reduces to  $P_{\text{ASE}} = \frac{1}{2} N(N+1) a_0$  for a flat comb and to  $P_{\text{ASE}} \simeq N a_0 / (1 - GT)$  for an exponentially decaying comb.

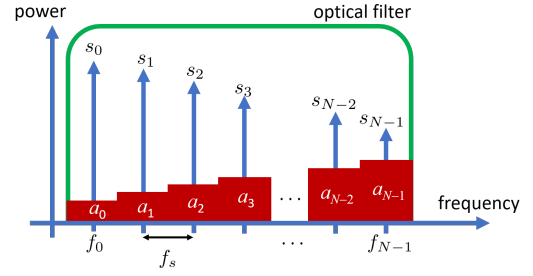


Fig. 2. Schematics of the optical spectrum of the FSL field with ASE: blue, power of the spectral lines; red, power of the ASE slices; green: schematic transmittance of the optical bandpass filter.

We define the comb's optical SNR as:

$$\text{OSNR} = \frac{P_{\text{comb}}}{P_{\text{ASE}}} \quad (8)$$

Thus, the OSNR values of the flat and exponentially decaying combs are, respectively:

$$\text{OSNR} = \frac{2}{N+1} \frac{s_0}{a_0} \quad GT \rightarrow 1 \quad (9)$$

and:

$$\text{OSNR} = \frac{1}{N} \frac{s_0}{a_0} \quad (GT)^N \ll 1 \quad (10)$$

In general, the OSNR is a function of the number of lines  $N$ , the  $GT$  product, and the quotient  $s_0/a_0$  that describes the ratio of injected power and the excess ASE power generated by the amplifier in single pass in a bandwidth of  $f_s$  and in a single polarization. Using typical values ( $s_0 = 1 \mu\text{W}$ ,  $a_0 = 0.1 \text{ nW}$ ) this ratio is 40 dB for an acousto-optics FSL, a figure that sets a scale for the values of SNR to be derived in the following sections. It can be shown, either analytically or by a simulation based on (3) and (7), that among all possible  $GT$  products below threshold,  $GT < 1$ , the OSNR is maximized by the flat comb and thus (9) represents its maximum value.

In the calculus of the SNR we will need some results from the coherence theory of the ASE generated by the FSL. We present these results here, leaving its justification to Appendix A. Due to the frequency shifting, both the ASE field  $\epsilon(t)$  and the ASE intensity  $I_\epsilon(t) = |\epsilon(t)|^2$  are cyclostationary noise processes. The intensity, however, has constant mean  $\langle I_\epsilon(t) \rangle = P_{\text{ASE}}$  since the recirculation round-trip delay  $\tau_c$  is typically larger than the ASE coherence time, and so the intensity of the sum of recirculating ASE fields is the sum of their intensities. Moreover, the ASE intensity shows photon bunching and in this regard it is similar to a stationary chaotic field despite being cyclostationary. This property is well understood in the related context of frequency-shifted feedback lasers [35], [36]. The degree of second-order coherence at zero lag is therefore:

$$g^{(2)}(0) = \frac{\langle I_\epsilon(t)^2 \rangle}{\langle I_\epsilon(t) \rangle^2} = 2 \quad (11)$$

This is equivalent to the following fourth-order correlation of the ASE field:

$$\langle I_\epsilon(t)^2 \rangle = \langle |\epsilon(t)|^4 \rangle = 2 \langle |\epsilon(t)|^2 \rangle^2 = 2 P_{\text{ASE}}^2 \quad (12)$$

On the other hand, the recirculation of the ASE field leads to partial correlations in the intensity at time lags multiples of the loop's round-trip time  $\tau_c$ . These correlations show up in the spectrum of intensity noise as bumps at frequencies multiples of  $1/\tau_c$ , an effect that, again, is well known in frequency-shifted feedback lasers [36]. Since the typical length of fiber loops is of the order of some or even tens of meters, the scale  $1/\tau_c$  lies in the MHz range. This implies that at least some noise bumps always enter the electrical detection bandwidth of practical receivers, which may range from the value of the optical bandwidth (tens of GHz using direct detection or self-heterodyne receivers) to a fraction of the shifting frequency (tens of MHz for dual-comb schemes). The only systematic means to avoid them, and thus optimize the SNR, is to employ balanced detection. This is the reason why most of the receivers analyzed below make use of this type of detectors. Our first scenario, however, is based on direct detection, for whose analysis it suffices the aforementioned result (12).

### III. SNR FOR FSL PEAK DETECTION

In the following paragraphs we address the computation of the SNR attainable by FSL fields in ASE-induced noise at a peak used for detection. This peak can result after the direct detection of an optical pulse or as a result of the correlation of a more general FSL waveform with a certain matched filter, this being implemented by optical or digital means. In the former case, the FSL is generally operated in an integer Talbot condition, so that the FSL output consists of a series of transform-limited pulses described as:

$$e(t) = \sum_{n=0}^{N-1} \sqrt{s_n} e^{i2\pi n f_s (t-\tau)} \quad (13)$$

In the latter case, the optical FSL waveforms are described, in general, by (1). Of course, the practical meaning of the peak and the appropriate system's performance metrics rely on the application under consideration. These issues, together with the expected impact of quantization noise, will be considered in Section IV. However, in order to justify the definitions used in the present section, we will assume that the FSL is used as a (coherent or incoherent) optical reflectometer, where an unknown chain of reflective events are placed after the FSL output and before detection.

#### A. Direct Detection

Following the scheme depicted in Fig. 3, we consider the direct detection of the pulse train (13) using a wideband detector with electrical bandwidth  $Nf_s$  equal to the comb's spectral width. The voltage after photodetection is

$$\begin{aligned} v(t) &= |e(t) + \epsilon(t)|^2 \\ &= |e(t)|^2 + [e(t)^* \epsilon(t) + e(t) \epsilon(t)^*] + |\epsilon(t)|^2 \\ &= v_S(t) + v_{SA}(t) + v_A(t) \end{aligned} \quad (14)$$

where, correspondingly,  $v_S(t)$  is the signal term representing the intensity of the transform-limited train of pulses, and  $v_{SA}(t)$  and  $v_A(t)$  are two noise terms originated, respectively,

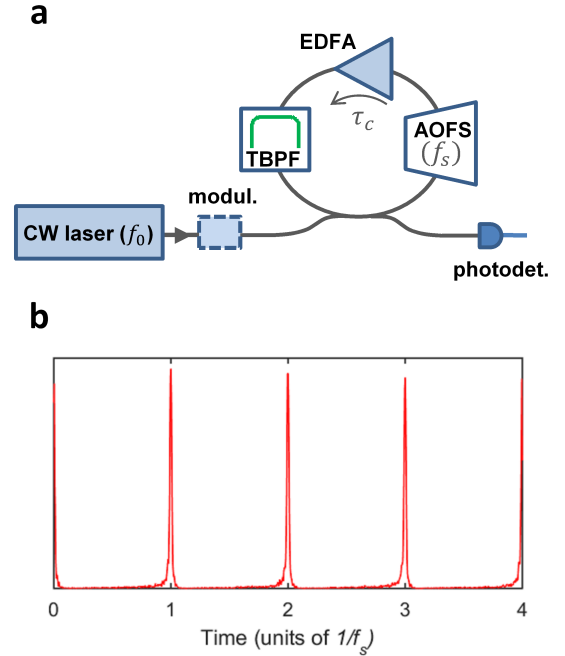


Fig. 3. a: Schematics of an acousto-optic FSL with direct detection. When used to perform the real-time Fourier transform of RF signals, an electro-optic modulator is placed after the CW laser. b: Simulation of the recorded voltage when the FSL is configured in an integer Talbot condition. The trace shows the intensity of a train of transform-limited pulses with period  $1/f_s$  in the presence of noise.

by the signal-ASE beat and by the ASE intensity. The average ASE intensity  $\langle v_A(t) \rangle = P_{ASE}$  provides a dc level for the voltage time trace  $v(t)$  whereas the signal-ASE beat  $v_{SA}(t)$  is of zero mean. The variance of this signal-ASE beat, however, depends on the time where it is evaluated and is proportional to the pulse intensity: it is high within the pulse duration and zero between pulses. Experimentally, the voltage trace  $v(t)$  entails a series of noisy peaks surrounded by a relatively quiet noise background due to ASE intensity noise only.

The SNRs used in this paper will be defined from the optical point of view, and so the signal power in its numerator is proportional to the optical power. This approach is particularly suited to situations where one wishes to compare a detected optical power level, for instance in an optical measurement system, with the relevant noise power level. This point of view contrasts with the conventional electrical definition of the SNR of optical communication systems, where the signal power is the electrical power delivered by the receiver.

In our case, we assume that the FSL pulse train is used in a reflectometric configuration, and so it works as an incoherent reflectometer: voltage  $v_S(t)$  represents a series of pulses whose peak values are proportional to the reflected intensity and so to the reflectivity. The SNR is thus given by the ratio between the voltage at the intensity peak and the rms values, denoted by tildes, of the noise voltages also evaluated at the peak:

$$\text{SNR}_{\text{peak}} = \frac{v_{S,\text{peak}}}{\sqrt{\tilde{v}_{SA,\text{peak}}^2 + \tilde{v}_A^2}} \quad (15)$$

Here,  $\tilde{v}_A$  is the rms value of the ASE intensity noise, which is

constant over time and hence can be described as a statistical or as a temporal average:

$$\tilde{v}_A = \langle v_A(t)^2 \rangle^{\frac{1}{2}} = \left( \frac{1}{T_a} \int^{T_a} dt v_A(t)^2 \right)^{\frac{1}{2}} \quad (16)$$

In turn,  $\tilde{v}_{SA,\text{peak}}$  is the rms value of the (time-dependent) signal-ASE beat  $\tilde{v}_{SA}(t) = \langle v_{SA}(t)^2 \rangle^{\frac{1}{2}}$  evaluated at the peak. This optical definition of SNR is standard in the analysis of incoherent reflectometers (see, for instance, [37] for conventional OTDR). The equivalent electrical SNR would simply be the square of the ratio in (15).

From (13), the peak voltage is:

$$v_{S,\text{peak}} = \max |e(t)|^2 = \left( \sum_{n=0}^{N-1} \sqrt{s_n} \right)^2 \equiv N_0 P_{\text{comb}} \quad (17)$$

where we have defined the equivalent number of lines  $N_0 = (\sum_n \sqrt{s_n})^2 / \sum_n s_n$ . It can be shown that  $1 \leq N_0 \leq N$  and that its maximum value of  $N$  is reached by the flat comb. For the signal-ASE beat at the peak we find

$$\begin{aligned} \tilde{v}_{SA,\text{peak}} &= \left( \sum_n \sqrt{s_n} \cdot \langle |\epsilon(t) + \epsilon^*(t)|^2 \rangle^{\frac{1}{2}} \right) \\ &= \sqrt{2N_0 P_{\text{comb}} P_{\text{ASE}}} \end{aligned} \quad (18)$$

where we have used the peak value of  $|e(t)|$ , the fact that  $\langle |\epsilon(t)|^2 \rangle = P_{\text{ASE}}$ , and that  $\langle \epsilon(t)^2 \rangle = \langle \epsilon(t)^*{}^2 \rangle = 0$  due to the circularity of the ASE field. Finally,  $\tilde{v}_A$  is constant and given by (12):

$$\tilde{v}_A = \langle |\epsilon(t)|^4 \rangle^{\frac{1}{2}} = \sqrt{2} P_{\text{ASE}} \quad (19)$$

The SNR thus writes:

$$\text{SNR}_{\text{peak}} = \frac{N_0 P_{\text{comb}}}{\sqrt{2N_0 P_{\text{comb}} P_{\text{ASE}} + 2P_{\text{ASE}}^2}} \simeq \sqrt{\frac{N_0 P_{\text{comb}}}{2P_{\text{ASE}}}} \quad (20)$$

where in the last approximation we have assumed that  $N_0 P_{\text{comb}} \gg P_{\text{ASE}}$ . For arbitrary values of the  $GT$  product, this SNR can be computed by use of (3) and (7). The SNR becomes optimal for the flat comb  $GT \rightarrow 1$  as it maximizes both  $N_0$  and the OSNR. The result is:

$$\max \text{SNR}_{\text{peak}} = \left( \frac{N}{N+1} \frac{s_0}{a_0} \right)^{\frac{1}{2}} \simeq \left( \frac{s_0}{a_0} \right)^{\frac{1}{2}} \quad (21)$$

where again we have used that  $N \gg 1$ . This optimal SNR is of the order of 20 dB as follows from our estimations of  $s_0$  and  $a_0$  in the previous section.

### B. Self-heterodyne Balanced Detection

This detection scheme represents the simplest coherent alternative to the previous receiver. Field (13) is mixed with a portion  $e_0 \exp(i2\pi f_0 t)$  of the CW seed acting as a local oscillator (LO), as is shown in Fig. 4. Its complex amplitude will be denoted by  $e_0 = \sqrt{P_{\text{LO}}} \exp(i\theta)$ , with  $P_{\text{LO}}$  the LO power and  $\theta$  the interferometer's phase imbalance. Photodetection is performed by use of a wideband balanced detector, again of bandwidth  $Nf_s$ . The computation proceeds along the same

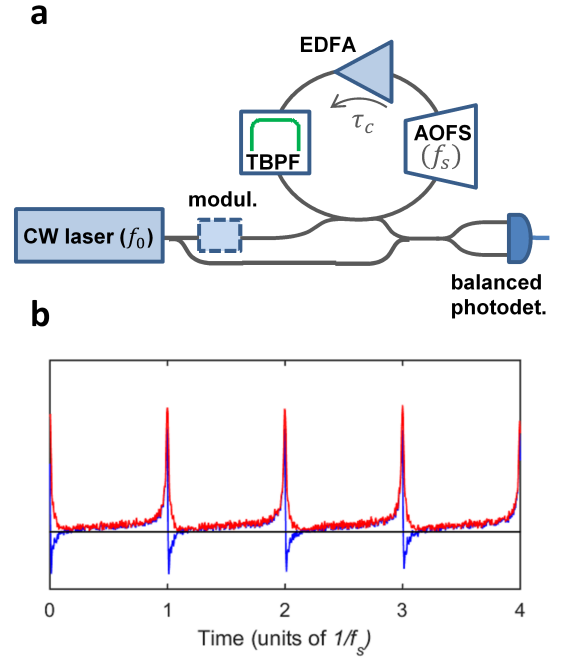


Fig. 4. a: Schematics of an acousto-optic FSL with balanced self-heterodyne detection. b: Simulation of the recorded voltage when the FSL is configured in an integer Talbot condition. The detected signal is a set of noisy oscillating waveforms with period  $1/f_s$ , in blue. Here, the interferometer is stabilized at phase imbalance  $\theta = \pi/3$  (see text). Hilbert transform can be used to realize an envelope detection, in red, which represents the amplitude of the transform-limited pulses.

lines as in direct detection, with only a significant difference in the definition of SNR. The voltage is:

$$\begin{aligned} v(t) &= [e_0^* e(t) + e_0 e(t)^*] + [e_0^* \epsilon(t) + e_0 \epsilon(t)^*] \\ &= v_S(t) + v_A(t) \end{aligned} \quad (22)$$

where, using a notation similar to that used in the previous subsection,  $v_S(t)$  and  $v_A(t)$  describe respectively the signal and the ASE noise terms. Noise  $v_A(t)$  is now purely additive and of zero mean, and generates a noise level constant over time. The resulting trace is a periodic series of peaked waveforms, as is also depicted in Fig. 4.

Given that in a coherent receiver such as the one treated here the signal term  $v_S(t)$  is proportional to the field's amplitude, and thus to the square root of the reflectivity, the SNR is:

$$\text{SNR}_{\text{peak}} = \frac{v_{S,\text{peak}}^2}{\tilde{v}_A^2} \quad (23)$$

Note the change with respect to the SNR defined in (15) for an incoherent reflectometer: here, the optical and the electrical definitions of SNR coincide. The peak value in (23) is:

$$\begin{aligned} v_{S,\text{peak}} &= \max |e_0^* e(t) + e_0 e(t)^*| = 2 |\cos \theta| \sqrt{P_{\text{LO}}} \sum_{n=1}^{N-1} \sqrt{s_n} \\ &\simeq 2 |\cos \theta| \sqrt{N_0 P_{\text{LO}} P_{\text{comb}}} \end{aligned} \quad (24)$$

Here we have excluded the  $n = 0$  spectral line in the sum, as it would lead to a constant background voltage that does not contribute to the peak determination. In practice, this is

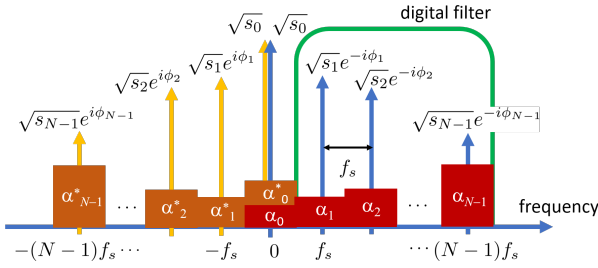


Fig. 5. Schematics of the contributions to the RF spectrum in self-heterodyne detection: blue (resp. yellow), power of the spectral lines in  $e(t)$  (resp.  $e^*(t)$ ); red (resp. brown), power of the ASE slices in  $e(t)$  (resp.  $e^*(t)$ ); green, schematic transmittance of the digital filter.

implemented by a dc-rejection filter applied to the voltage trace. The rms noise level is:

$$\tilde{v}_A = \langle [e_0^* \epsilon(t) + e_0 \epsilon(t)^*]^2 \rangle^{\frac{1}{2}} = \sqrt{2P_{LO}P_{ASE}} \quad (25)$$

The SNR at the peak finally writes:

$$\text{SNR}_{\text{peak}} = \frac{2 \cos^2 \theta N_0 P_{\text{comb}}}{P_{ASE}} \leq 4 \cos^2 \theta \frac{s_0}{a_0} \quad (26)$$

The bound presented in the last part of the equation corresponds to the flat comb in the limit of large  $N$ , and shows a typical value of 46 dB when the interferometer is stabilized at imbalances  $\theta = 0$  or  $\pi$ . This SNR represents a significant increase with respect to direct detection that is consequence of the coherent character of the receiver.

Other alternatives for peak determination result in a decrease of SNR. First, peak detection can be performed by averaging over different phase imbalances with a subsequent deterioration of the SNR by 3 dB since  $\langle \cos^2 \theta \rangle = \frac{1}{2}$ . The same loss is observed if one uses IQ demodulation and considers the square modulus [38]. Peak detection can alternatively be performed by purely digital means, taking advantage of the single-sided character of the FSL optical spectrum [12]. As a real signal, the spectrum of  $v(t)$  is double-sided with a bandwidth equal to the comb's optical width, as is schematically depicted in Fig. 5. This voltage is first dc-filtered and then Hilbert transformed to remove negative frequencies, as is also shown in that figure. This filtering procedure will be denoted by a caret in what follows. The filtered voltage is then given by  $\hat{v}(t) = e_0^*[\hat{e}(t) + \hat{\epsilon}(t)]$  and the peak amplitude becomes independent of the interferometer's imbalance:

$$|\hat{v}_S|_{\text{peak}} = \max |e_0^* \hat{e}(t)| = \sqrt{P_{LO}} \sum_{n=1}^{N-1} \sqrt{s_n} \quad (27)$$

The peak amplitude is thus halved as compared with (24) for  $\theta = 0, \pi$ , and so the signal power is divided by a factor of four. On the other hand, the noise power is halved after filtering negative frequencies, resulting again in a 3-dB SNR loss.

### C. Digital Pulse Compression

Correlation or pulse-compression techniques aim at the detection of a noisy optical waveform through the correlation with a specific (reference) waveform. As a result, the energy of the original waveform is gathered in the form of a virtual

pulse that is used for detection. The optimal reference is defined as the specific waveform that maximizes the SNR at the correlation peak. In the simplest case where noise is white, the optimal correlation is performed with the noiseless waveform. In the case at hand, the objective is to detect the periodic sequence of optical waveforms (1) generated by the FSL. Such a procedure results in the cyclic autocorrelation of the FSL field:

$$R_e(t) = f_s \int_0^{T_s} du e(u)^* e(u+t) = \sum_{n=0}^{N-1} s_n e^{i2\pi n f_s t} \quad (28)$$

where we have denoted by  $T_s = 1/f_s$  the period of the FSL train. This series of autocorrelation peaks does not depend on the actual temporal waveform, only on the power  $s_n$  of the optical spectral lines. This observation, which is equivalent to the Wiener-Khinchin theorem, allows for the detection of more general waveforms than the transform-limited pulse trains used in the previous subsections. This fact represents an advantage in reflectometric-type systems where the FSL output is to be amplified before probing an optical circuit, since the generic FSL field (1) contains families of quasi-CW waveforms [12].

We consider the digital pulse compression procedure used in [12]. This technique is based on a self-heterodyne receiver, and so the starting point of our analysis is (22). Again, as shown in Fig. 5, this voltage is first dc-filtered up to frequency  $f_s/2$  and then Hilbert transformed to remove negative frequencies. The complex voltage can be expressed in terms of slices as:

$$\begin{aligned} \hat{v}(t) &= \hat{v}_S(t) + \hat{v}_A(t) = e_0^* [\hat{e}(t) + \hat{\epsilon}(t)] = \\ &= \sqrt{P_{LO}} e^{-i\theta} \sum_{n=1}^{N-1} [\sqrt{s_n} e^{-i\phi_n} + \alpha_n(t)] e^{i2\pi n f_s t} \quad (29) \end{aligned}$$

The noise term  $\hat{v}_A(t)$  is proportional to the filtered ASE  $\hat{\epsilon}(t)$  so that its  $n = 0$  slice is also absent. The signal term  $\hat{v}_S(t)$  is proportional to the dc-filtered FSL field  $\hat{e}(t)$ , which can be expressed as a periodic series of waveforms  $w(t)$ :

$$\hat{e}(t) = \sum_{n=1}^{N-1} \sqrt{s_n} e^{-i\phi_n} e^{i2\pi n f_s t} = \sum_{k=-\infty}^{+\infty} w(t - kT_s) \quad (30)$$

As is well-known, the impulse response  $h_w(t)$  of the filter matched to the detection of  $w(t)$  is contained in the interval  $[0, T_s]$  and given by  $h_w(t) = f_s \cdot w(T_s - t)^*$ . It can be alternatively expressed in terms of the periodic field  $\hat{e}(t)$  provided that this field is restricted to a fundamental period:

$$h_w(t) = f_s \cdot \hat{e}(-t)^* \quad 0 \leq t \leq T_s \quad (31)$$

However, this standard matched filter is not optimal, since ASE noise is not white. Instead of relying on the general theory of matched filtering in non-white noise, we construct the optimal filter using a simple generalization of (31). We consider a family of impulse responses given by:

$$h(t) = f_s \sum_{n=1}^{N-1} h_n \sqrt{s_n} e^{i\phi_n} e^{i2\pi n f_s t} \quad 0 \leq t \leq T_s \quad (32)$$

with non-negative weights  $h_n \geq 0$  to be optimized. The standard matched filter (31) corresponds to  $h_n = 1$ . The result

of the convolution of  $\hat{v}(t)$  with (32), denoted as  $r(t)$ , is also composed of signal and additive noise:

$$r(t) = r_S(t) + r_A(t) = h(t) \otimes \hat{v}(t) \quad (33)$$

Using (30) and (32) the convolution can be written as:

$$r(t) = \sqrt{P_{\text{LO}}} e^{-i\theta} \sum_{n=1}^{N-1} [h_n s_n + \beta_n(t)] e^{i2\pi n f_s t} \quad (34)$$

We observe that only in the specific case of the standard matched filter, the signal term is proportional to the field's autocorrelation (28) except for the absence of the first ( $n = 0$ ) spectral line. For arbitrary  $h_n$  the signal term still gives a series of cross-correlation peaks with amplitude:

$$|r_S|_{\text{peak}} = \sqrt{P_{\text{LO}}} \sum_{n=1}^{N-1} h_n s_n \quad (35)$$

that can be alternatively used for detection.

As for the noise in (34), we show that the random functions  $\beta_n(t)$  have their frequency content in the interval  $[-f_s/2, f_s/2]$ , and therefore they describe fluctuations in the correlation's harmonics. Indeed, after performing the convolution  $\beta_n(t)$  can be expressed as:

$$\beta_n(t) = h_n \sqrt{s_n} e^{i\phi_n} f_s \int_{t-T_s}^t du \hat{\epsilon}(u) e^{-i2\pi n f_s u} \quad (36)$$

Hence,  $\beta_n(t)$  is proportional to a causal running average over a time scale  $T_s = 1/f_s$ , which represents a low-pass filter of bandwidth  $f_s/2$ . The integrand in (36) is the filtered ASE field,  $\hat{\epsilon}(u)$ , downshifted in frequency by  $n f_s$ . According to (4), the portion of this downshifted field that passes through the running average filter is the  $n$ -th slice of ASE,  $\alpha_n(t)$ . Fluctuations  $\beta_n(t)$  are therefore ASE slices weighted by the corresponding harmonics of the filter:

$$\beta_n(t) \simeq h_n \sqrt{s_n} e^{i\phi_n} \alpha_n(t). \quad (37)$$

The ASE slices  $\alpha_n(t)$  are described by circular gaussian stationary noise processes with zero mean. Moreover, we show in Appendix A that different slices are mutually uncorrelated at equal times. These properties are inherited by fluctuations  $\beta_n(t)$ , so that  $\langle \beta_n(t)^* \beta_m(t) \rangle = \delta_{nm} \langle |\beta_n(t)|^2 \rangle$  and:

$$\langle |\beta_n(t)|^2 \rangle = h_n^2 s_n \langle |\alpha_n(t)|^2 \rangle = h_n^2 s_n a_n \quad (38)$$

Then, the (squared) rms noise level writes:

$$\begin{aligned} \tilde{r}_A^2 &= \langle |r_A(t)|^2 \rangle = \langle \left| \sqrt{P_{\text{LO}}} e^{-i\theta} \sum_{n=1}^{N-1} \beta_n(t) e^{i2\pi n f_s t} \right|^2 \rangle \\ &= P_{\text{LO}} \sum_{n=1}^{N-1} \langle |\beta_n(t)|^2 \rangle = P_{\text{LO}} \sum_{n=1}^{N-1} h_n^2 s_n a_n \end{aligned} \quad (39)$$

As a coherent reflectometer, the peak SNR is again given by the squares of signal and noise voltages, and so:

$$\text{SNR}_{\text{peak}} = \frac{|r_S|_{\text{peak}}^2}{\tilde{r}_A^2} = \frac{\left( \sum_{n=1}^{N-1} h_n s_n \right)^2}{\sum_{n=1}^{N-1} h_n^2 s_n a_n} \quad (40)$$

This SNR can be optimized using standard arguments: introducing the parametrization  $h_n = g_n \sqrt{a_0/a_n s_n}$  with unknown  $g_n \geq 0$  and using the Schwarz inequality we are led to:

$$\text{SNR}_{\text{peak}} = \frac{\left( \sum_{n=1}^{N-1} g_n \sqrt{\frac{a_0 s_n}{a_n}} \right)^2}{a_0 \sum_{n=1}^{N-1} g_n^2} \leq \sum_{n=1}^{N-1} \frac{s_n}{a_n} \quad (41)$$

where this maximum is attained for:

$$g_n = \sqrt{\frac{a_0 s_n}{a_n}} \implies h_n = \frac{a_0}{a_n} \quad (42)$$

and therefore the optimal filter de-emphasizes those signal harmonics which are more perturbed by noise. Notice that, if ASE were white ( $a_n = a_0$  for all  $n$ ), we would recover the definition of the standard matched filter. On the other hand, a simulation of the optimum value in (41) over different values of the  $GT$  product shows that the SNR is maximum, once more, in the case of a flat comb, for which  $s_n = s_0$  for all  $n$  and  $a_n = (n+1)a_0$ . In this case the SNR reads:

$$\max \text{SNR}_{\text{peak}} = \sum_{n=1}^{N-1} \frac{s_n}{a_n} = \frac{s_0}{a_0} \sum_{n=1}^{N-1} \frac{1}{n+1} \equiv \eta \frac{s_0}{a_0} \quad (43)$$

where, according to the asymptotic limit of the harmonic series,  $\eta = (\gamma - 1) + \log(N-1) + \mathcal{O}(1/N)$  with  $\gamma = 0.5772 \dots$  the Euler's constant. Noticeably, the optimal SNR increases logarithmically with the number of lines  $N$ , showing that under optimal matched filter detection it is beneficial to extend the FSL bandwidth despite the concomitant increase in ASE power. For a typical value  $N = 200$  we get  $\eta = 4.87$ , which amounts to 6.9 dB above the  $s_0/a_0$  level. Comparison with (26) shows that the typical improvement with respect to a self-heterodyne receiver with peak determination based on averaged imbalances, IQ demodulation, or digital techniques is  $\sim 4$  dB, an improvement that decreases to only  $\sim 1$  dB with respect to self-heterodyne detection with a stable interferometer imbalance  $\theta = 0, \pi$ . In this regard, the advantage of digital pulse compression is that it provides an equivalent SNR without the need of interferometer's stabilization.

Finally, we compute the suboptimal SNR that is reached when we use a standard matched filter ( $h_n = 1$ ) with the non-white ASE field. From (40) and assuming a flat comb in the limit of large  $N$ , we get:

$$\text{SNR}_{\text{peak}} = \frac{\left( \sum_{n=1}^{N-1} s_n \right)^2}{\sum_{n=1}^{N-1} s_n a_n} = \frac{s_0 (N-1)^2}{a_0 \left[ \frac{1}{2} N(N+1) - 1 \right]} \simeq 2 \frac{s_0}{a_0} \quad (44)$$

This SNR is independent of the number of spectral lines, showing that there is no improvement with an additional increase in FSL bandwidth. In practical situations, the SNR is degraded by  $\sim 4$  dB with respect to the detection with an optimal filter (43), and is thus equivalent to a self-heterodyne receiver with peak determination based on averaged imbalances, IQ demodulation, or digital techniques.

### D. Analog Pulse Compression using Dual Comb

In a dual-comb correlation receiver [13], schematically shown in Fig. 6, the field's correlation is retrieved by use of a second optical comb which provides, at the same time, line-by-line self heterodyne detection together with down-conversion. The initial comb, referred to as the probe and denoted as before by  $e(t)$ , is used to explore a certain optical circuit (not shown in the figure). The description of this comb is given by (1) together with the ASE slices (4). The additional comb, designated as the reference, exhibits the same form and the same set of spectral phases  $\phi_n$  as the probe and will be denoted with primes. Without loss of generality we assume that both combs have the same number of spectral lines  $N$ . The reference field is:

$$e'(t) + \epsilon'(t) = \sum_{n=0}^{N-1} h_n \left[ \sqrt{s'_n} e^{-i\phi'_n} + \alpha'_n(t) \right] e^{i2\pi n f'_s (t-\tau)} \quad (45)$$

with  $s'_n$  the power of the spectral lines and  $a'_n = \langle |\alpha'_n(t)|^2 \rangle$  the ASE slice power. The ASE from these two combs represents a pair of independent noise sources in the correlation receiver. The repetition rate  $f'_s$  of the reference is close but not equal to that of the probe,  $f_s$ . We assume that  $f_s > f'_s$ , and denote  $\Delta f = f_s - f'_s$ . This figure is low, typically some tens of kHz. Also, and motivated by the result of the previous subsection, we assume that before optical mixing we introduce an optical filter in the reference comb to be used for SNR optimization, described in (45) by weights  $h_n \geq 0$ .

The two fields are sent to a slow balanced detector with bandwidth  $B$  of the order of  $N\Delta f$  and such that  $B < f_s/2, f'_s/2$ . The detected voltage is:

$$v(t) = [(e(t) + \epsilon(t))(e'(t)^* + \epsilon'(t)^*) + (e(t)^* + \epsilon(t)^*)(e'(t) + \epsilon'(t))]_{lp} \quad (46)$$

The subindex  $lp$  is used to denote the low-pass filtering implemented by the slow balanced detector. As is also shown in Fig. 6, the detected signal is a set of (noisy) peaks with period  $1/\Delta f$ . In the absence of ASE noise they constitute the signal term in (46). Noticing the action of the low-pass filter, this signal term is given by:

$$\begin{aligned} v_S(t) &= [e(t)e'(t)^* + e(t)^*e'(t)]_{lp} \\ &= 2 \sum_{n=1}^{N-1} h_n \sqrt{s_n s'_n} \cos(2\pi n \Delta f t) \end{aligned} \quad (47)$$

which is (twice) the real part of the cyclic cross-correlation of both combs with period  $1/\Delta f$ . In the specific case of equal weights,  $h_n = 1$ , and equal fields,  $s_n = s'_n$ , we recover the autocorrelation (28). Note that we have excluded again the first spectral line ( $n = 0$ ) by setting  $h_0 = 0$ . This also rejects the  $n = 0$  terms in the ASE noise levels analyzed below. In general, the signal's peak value is:

$$v_{S,peak} = 2 \sum_{n=1}^{N-1} h_n \sqrt{s_n s'_n} \quad (48)$$

The rest of the terms arising in (46) are noise sources for the detected voltage. They can be grouped in pairs, corresponding

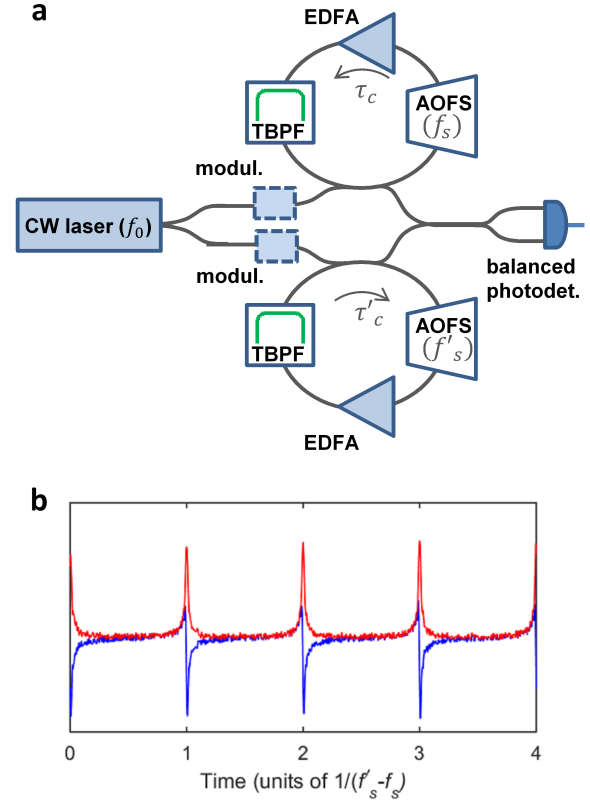


Fig. 6. a: Schematics of a dual-comb correlation receiver based on two acousto-optic FSLs and a balanced detector, followed by a low-pass filter (LP). For the probe (resp.: reference) comb, the frequency shift per roundtrip is equal to  $f_s$  (resp.:  $f'_s$ ), and the roundtrip time to  $\tau_c$  (resp.  $\tau'_c$ ). b: Simulation of the recorded voltage. The detected signal is a set of noisy oscillating waveforms with period  $1/\Delta f$ , in blue. Here, the interferometer is stabilized at phase imbalance  $\theta = 2\pi/3$  (see text). Hilbert transform can be used to realize an envelope detection, in red.

to reference-ASE, probe-ASE, and ASE-ASE beat terms. The detailed computation of their rms noise levels is presented in Appendix B; here we only show the results. The first pair describes the beat between the reference comb and the ASE in the probe comb, and the second is the analogous probe-ASE beat. They are respectively given by:

$$\begin{aligned} v_{S'A}(t) &= [e'(t)\epsilon(t)^* + e'(t)^*\epsilon(t)]_{lp} \\ v_{SA'}(t) &= [e(t)\epsilon'(t)^* + e(t)^*\epsilon'(t)]_{lp} \end{aligned} \quad (49)$$

The (squared) rms noise levels are:

$$\tilde{v}_{S'A}^2 = \frac{4B}{f_s} \sum_{n=1}^{N-1} h_n^2 s'_n a_n \quad \tilde{v}_{SA'}^2 = \frac{4B}{f'_s} \sum_{n=1}^{N-1} h_n^2 s_n a'_n \quad (50)$$

and involve the weighted product of spectral line's power and ASE slice power. The final pair of noise terms entails the ASE-ASE beat:

$$v_{AA'}(t) = [\epsilon(t)\epsilon'(t)^* + \epsilon(t)^*\epsilon'(t)]_{lp} \quad (51)$$

and its rms value is given by a weighted product of ASE slice powers:

$$\tilde{v}_{AA'}^2 = \frac{4B}{f_s} \sum_{n=1}^{N-1} h_n^2 a_n a'_n \quad (52)$$

Using (48), (50) and (52) and recalling that  $f_s \simeq f'_s$ , the peak SNR can be written as:

$$\text{SNR}_{\text{peak}} = \frac{v_{S,\text{peak}}^2}{\tilde{v}_{S'A}^2 + \tilde{v}_{S'A'}^2 + \tilde{v}_{AA'}^2} \quad (53)$$

$$= \frac{f_s}{B} \frac{\left( \sum_{n=1}^{N-1} h_n \sqrt{s_n s'_n} \right)^2}{\sum_{n=1}^{N-1} h_n^2 (s'_n a_n + s_n a'_n + a_n a'_n)}$$

It can be optimized using the same technique as in the previous subsection. The optimal SNR is given by:

$$\max \text{SNR}_{\text{peak}} = \frac{f_s}{B} \sum_{n=1}^{N-1} \frac{s_n s'_n}{s'_n a_n + s_n a'_n + a_n a'_n} \quad (54)$$

which is attained by a de-emphasis filter defined by the weights:

$$h_n = \frac{2a_0 \sqrt{s_n s'_n}}{s'_n a_n + s_n a'_n + a_n a'_n} \quad (55)$$

These general expressions can be particularized to specific situations. In general, one can simplify them by neglecting the ASE-ASE beat because  $a_n, a'_n \ll s_n, s'_n$ . Moreover, in some instances both probe and reference combs are similar. This is the case of bidirectional FSL [13] where the reference and the probe combs travel in the same TBPF, and where both the optical spectral lines and the ASE slice powers are equal,  $s_n = s'_n$  and  $a_n = a'_n$ . In this situation we get a de-emphasis filter given by the same set of weights as in digital pulse compression,  $h_n = a_0/a_n$ , and an optimal SNR of

$$\max \text{SNR}_{\text{peak}} = \frac{f_s}{2B} \sum_{n=1}^{N-1} \frac{s_n}{a_n} \quad (56)$$

which therefore shows an improvement with respect to (43) by  $f_s/2B$ . This ratio represents the product of a bandwidth compression factor,  $f_s/B$ , detached by a factor of 2 that accounts for the doubling of ASE noise, present in both the probe and the reference combs. This factor can be significant: using typical values ( $f_s = 80$  MHz,  $B = 4$  MHz), the expected SNR increase is 10 dB. However, this improvement comes at the expense of detection speed since, as is shown by (47), the correlation update period is  $1/\Delta f$  instead of the value  $1/f_s$  in the digital correlation technique. Using these values with the estimation provided after (43), the typical optimal SNR can be as large as 56.9 dB, i.e., 16.9 dB above the  $s_0/a_0$  level.

Another relevant limit of the general expression (53) is that describing a situation where both combs are similar and flat, but the reference comb is not optimized ( $h_n = 1$ ). Again, we assume that the ASE-ASE beat is negligible. The suboptimal SNR given by (53) is:

$$\text{SNR}_{\text{peak}} = \frac{f_s}{B} \frac{s_0}{a_0}. \quad (57)$$

With the typical values of  $f_s$  and  $B$  given before, this amounts to 13 dB above the  $s_0/a_0$  level and  $\sim 4$  dB below the optimal SNR, a degradation similar to that found with digital correlation techniques.

## IV. APPLICATIONS

### A. Coherent Optical Reflectometry

The ASE-limited SNR values derived for the different receivers so far are summarized in the first line of Table I. As pointed out before, all these receivers, except the direct detection scheme, can be used in coherent reflectometry systems. Their SNR, understood as a relative ASE noise level accompanying the probe field, comes with any detected reflection. In consequence, the SNR coincides with the dynamic range (DR) of a reflectometric measurement, this being defined as the maximum ratio between two simultaneously detectable reflectivities. The minimum detectable reflectivity  $R_{\text{min}}$  or (reflectometric) sensitivity, however, is not determined by ASE, but by the local oscillator's power  $P_{\text{LO}}$ , the optical comb's power  $P_{\text{comb}}$ , and the receiver electronics noise. We derive sensitivity estimates for FSL systems employing flat combs under standard assumptions.

Let us first consider a FSL reflectometer based on self-heterodyne balanced detection of transform-limited pulses. For sufficient local oscillator power, typically some milliwatts, detection is limited by the shot noise  $I_{sh}(t)$  generated by the local oscillator [39]. The one-sided, shot-noise current spectral density is given by  $i_{sh}^2(f) = 2e\mathcal{R}P_{\text{LO}}$ , with  $e$  the electron's charge and  $\mathcal{R}$  the photodiode's responsivity. The FSL comb, assumed flat and of bandwidth  $Nf_s$ , reaches the detector with a power  $RP_{\text{comb}}$ , where  $R$  is the reflectivity. The signal at the peak (24), expressed as a photocurrent, is  $2\mathcal{R}|\cos\theta|\sqrt{NR P_{\text{LO}} P_{\text{comb}}}$ , and therefore the sensitivity at  $\text{SNR} = 1$  is:

$$R_{\text{min}} = \frac{1}{\cos^2\theta} \frac{i_{sh}^2 f_s}{4\mathcal{R}^2 P_{\text{LO}} P_{\text{comb}}} = \frac{1}{\cos^2\theta} \frac{e f_s}{2\mathcal{R} P_{\text{comb}}} \quad (58)$$

Using typical values,  $\mathcal{R} = 0.9$  A/W and  $P_{\text{comb}} = 100 \mu\text{W}$ , this yields  $R_{\text{min}} = -71$  dB for  $\theta = 0, \pi$  and  $-68$  dB for the alternative peak detection methods.

The sensitivity of a shot-noise limited reflectometer based on a heterodyne receiver with digital pulse compression can be computed from (40) as follows. The digitally filtered signal voltage in (29) with added shot noise can be presented as:

$$\hat{v}(t) = Z \left( \mathcal{R} e_0^* \hat{e}(t) + \hat{I}_{sh}(t) \right) = Z \mathcal{R} e_0^* \left( \hat{e}(t) + \frac{\hat{I}_{sh}(t)}{\mathcal{R} e_0^*} \right) \quad (59)$$

where  $Z$  is the detector's impedance. Here, the caret on the shot-noise current  $\hat{I}_{sh}(t)$  denotes that only positive frequencies are to be considered. Hence, its current spectral density is halved,  $\hat{i}_{sh}^2(f) = i_{sh}^2(f)/2$ . In view of the structure of (59), it follows that shot noise generates single-sided white noise with constant spectral density  $i_{sh}^2/2\mathcal{R}^2 P_{\text{LO}} = e/\mathcal{R}$ , now in units of optical power per hertz. Then, the SNR is that given by (40) after the substitution of  $a_n$  with a constant slice power  $a_{sh} = i_{sh}^2 f_s / 2\mathcal{R}^2 P_{\text{LO}}$ . Using also that for a flat comb returned from a reflector  $s_n = RP_{\text{comb}}/N$  this directly leads to:

$$R_{\text{min}} = \frac{N \sum_n h_n^2}{\left( \sum_n h_n \right)^2} \frac{i_{sh}^2 f_s}{2\mathcal{R}^2 P_{\text{LO}} P_{\text{comb}}} = \frac{N \sum_n h_n^2}{\left( \sum_n h_n \right)^2} \frac{e f_s}{\mathcal{R} P_{\text{comb}}} \quad (60)$$

TABLE I  
PERFORMANCE PARAMETERS OF FSL SYSTEMS<sup>a</sup>

	Direct detect.	Self-het. detection <sup>b</sup>	Digital pulse compression <sup>c</sup>	Dual comb <sup>c,d</sup>
SNR (dB)	20	46	43	47
Coherent optical reflectometry				
DR (dB)	–	46	43	47
R <sub>min</sub> (dB)	–	–71	–68	–61
Real-time Fourier transform of RF signals				
CDR (dB)	32	40	37	41
S (dBm)	–23	–30	–27	–31

<sup>a</sup> For  $s_0/a_0 = 40$  dB and flat combs with  $f_s = 80$  MHz and  $N = 200$ .

<sup>b</sup> With stabilized interferometer (left column) and alternative peak detection methods (right column).

<sup>c</sup> Filter matched to ASE (left column) and to white noise (right column).

<sup>d</sup> Bandwidth  $B = 4$  MHz.

The prefactor is unity at large  $N$  when the filter is matched to white noise,  $h_n = 1$ , and so the sensitivity becomes similar to the self-heterodyne receiver with the alternative peak detection methods. However, when the filter is matched to ASE-induced noise,  $h_n \sim 1/(n+1)$ , the prefactor becomes  $N\kappa/\eta^2$ , with  $\eta$  given in (43) and  $\kappa = \sum_{n=1}^{N-1} 1/(n+1)^2 \simeq \frac{\pi^2}{6} - 1$  in the limit of large  $N$ . For a typical value  $N = 200$ , this factor results in a deterioration of sensitivity by 10.4 dB with respect to self-heterodyne detection with a stabilized interferometer, or by 7.4 dB with the rest of peak detection methods. This reflects a compromise between DR and sensitivity: the receiving filter  $h_n$ , if matched to the white shot noise, maximizes sensitivity but not DR and, if matched to the non-white ASE-induced noise, maximizes DR but not sensitivity.

In a dual-comb correlation systems, the shot noise limit is more difficult to attain as the role of local oscillator is played by a second (reference) comb whose typical output power is below the milliwatt. This fact can be compensated by the increase in SNR associated to the decrease in detection bandwidth. Systems are typically limited by the receiver electronics noise, usually a transimpedance front-end whose noise spectral density  $i_e$  is dominated by thermal noise in the feedback resistor and by amplifier noise [37], [39]. From (48), the photocurrent generated in the balanced detector by a pair of flat combs with equal power  $P_{\text{comb}}$ , one of which returns to the receiver after a reflectivity  $R$  and the other weighted by  $h_n$ , is  $2\mathcal{R}\sqrt{R}P_{\text{comb}}(\sum_n h_n)/N$ . The noise power is simply  $i_e^2 B$ , with  $B$  the detection bandwidth. At SNR = 1 this yields a sensitivity of:

$$R_{\min} = \frac{N^2}{(\sum_n h_n)^2} \frac{i_e^2 B}{4\mathcal{R}^2 P_{\text{comb}}} \quad (61)$$

Comparison with the first expression in (60) shows that the prefactor is again unity for  $h_n = 1$ , but in general differs by  $\sum_n h_n^2/N = \kappa/N$ . This ratio is the power loss experienced by the flat reference comb after filtering with weights  $h_n$  and represents a comparative loss of sensitivity. With  $B = 4$  MHz and  $i_e = 2$  pA/ $\sqrt{\text{Hz}}$  together with the previously quoted values of  $\mathcal{R}$ ,  $N$  and  $P_{\text{comb}}$ , the actual sensitivity is  $R_{\min} = -60.8$  dB for a filter matched to ASE-induced noise,  $h_n \sim 1/(n+1)$ .

The advantage provided by the low detection bandwidth is therefore wasted by the reduction in reference comb's power. In turn, low-bandwidth detection with two flat combs, i.e., with  $h_n = 1$ , reaches a sensitivity of  $-93.1$  dB, largely surpassing the performance of wideband self-heterodyne systems even at the shot noise limit.

### B. Real-time Fourier Transforms of RF Signals

FSLs perform real-time Fourier transforms of arbitrary RF signals by exploiting the dependence of the FSL's output delay in the seed frequency [17]. Before the FSL, which is configured in an integer Talbot condition, the seed CW optical carrier at frequency  $f_0$  is modulated in amplitude by a RF signal  $v_{\text{RF}}(t)$ . If such a RF signal is a pure tone at frequency  $f_{\text{RF}}$  and amplitude  $v_0$ , thus of the form  $v_{\text{RF}}(t) = v_0 \sin(2\pi f_{\text{RF}} t)$ , the CW carrier develops optical sidebands at frequencies  $f_0 \pm f_{\text{RF}}$  that act as additional seed frequencies for the FSL. Each of these sidebands are then mapped to the time domain by the time delay  $\tau$  in (13), and as a result the output shows two transform-limited satellite pulses at delays  $\pm f_{\text{RF}}\tau_c/f_0$  relative to the main pulse created by the CW carrier. Assuming that the RF tone is impressed onto the carrier by use of a Mach-Zehnder modulator biased at quadrature, the optical power of each sideband seed is:

$$s'_0 = s_0 \frac{\pi^2}{2} \frac{Z_m}{V_\pi^2} P_{\text{RF}} \quad (62)$$

with  $Z_m$  the modulator's input impedance,  $V_\pi$  the modulator's half-wave voltage, and  $P_{\text{RF}} = v_0^2/2Z_m$  the input RF power. This linear relationship assumes absence of compression in the input modulator. Note that in this type of systems the input signal is a RF signal, and therefore the SNR is defined as a ratio where the numerator is an RF power. However, (62) states that the RF power is proportional to the optical power, and so the relevant SNRs are again given by (15), (23), (40) or (53), depending on the receiver under consideration.

In the case of a direct-detection receiver, the calculus of the SNR at the sideband-generated peak is immediate as it only entails the substitution in the first expression in (20) of  $P_{\text{comb}}$  with the power  $P'_{\text{comb}}$  of the comb generated by the sideband seed (62):

$$P'_{\text{comb}} = \sum_{n=1}^{N-1} (GT)^n s'_0 = \frac{\pi^2}{2} \frac{Z_m}{V_\pi^2} P_{\text{RF}} P_{\text{comb}} \quad (63)$$

The sensitivity  $S$  at SNR = 1, i.e. the input RF power at  $f_{\text{RF}}$  for which the sideband-generated pulse shows SNR = 1, is:

$$S = \frac{2(1 + \sqrt{3})}{\pi^2} \frac{V_\pi^2}{Z_m} \frac{P_{\text{ASE}}}{N_0 P_{\text{comb}}} \simeq \frac{1 + \sqrt{3}}{\pi^2} \frac{V_\pi^2}{Z_m} \frac{a_0}{s_0} \quad (64)$$

where the rightmost part of the equation is the asymptotic value of  $S$  for a flat comb with  $N \gg 1$ . The sensitivity is therefore inversely proportional to the OSNR and depends through the prefactor on the electro-optic modulator's characteristics. Using standard values of a low- $V_\pi$  modulator ( $Z_m = 50 \Omega$ ,  $V_\pi = 3$  V), the typical best-case value is  $S = -23.0$  dBm.

An additional metrics is the linear or compression dynamic range (CDR) [4], which is defined as the range of input

RF powers under which the output satellite pulse is above noise, and where its peak power is compressed by 1 dB or less relative to a linear response. In the present scheme, compression is determined by the input modulator for which the input RF power for 1 dB compression is given by [4]:

$$P_{1\text{dB}} = \frac{\phi_{1\text{dB}}^2 V_\pi^2}{2\pi^2 Z_m} \quad (65)$$

with  $\phi_{1\text{dB}} = 0.9504$ . Then, the CDR is given by:

$$\text{CDR} = \frac{P_{1\text{dB}}}{S} = \frac{\phi_{1\text{dB}}^2 V_\pi^2}{2(1 + \sqrt{3}) a_0} \frac{s_0}{a_0} = 0.1653 \frac{s_0}{a_0} \quad (66)$$

The optimal CDR is therefore  $-7.8$  dB below the ratio  $s_0/a_0$ , with a typical maximum value of  $\sim 32$  dB.

Real-time Fourier transform systems can also be implemented using any of the coherent receivers analyzed before, as they only entail the detection of the satellite peak generated by the modulation sideband. The values of sensitivity and CDR can be computed using the same arguments. In the case of self-heterodyne detection, and starting from (26), the sensitivity for  $\theta = 0, \pi$  reads

$$S = \frac{1}{\pi^2} \frac{V_\pi^2}{Z_m} \frac{P_{\text{ASE}}}{N_0 P_{\text{comb}}} \simeq \frac{1}{2\pi^2} \frac{V_\pi^2}{Z_m} \frac{a_0}{s_0} \quad (67)$$

where in the last part of the equation we have written again the sensitivity for a flat comb. Comparison with (64) results in an improvement by a factor of  $2(1 + \sqrt{3})$  or 7.4 dB, which reduces to 4.4 dB if the alternative peak determination methods are used instead. The same improvements are transferred to the CDR. The calculus for the remaining correlation receivers follow the same lines and, as shown in Table I, results in the same pattern of improvement and degradation of parameters as the SNR.

### C. Quantization Noise

Finally, we briefly discuss the limits imposed by quantization noise in the detection of FSL temporal waveforms. The signal to quantization noise ratio (SQNR) for a waveform with a given peak-to-average power ratio (PAPR) and displayed at full scale is, expressed in dB [40]:

$$\text{SQNR} = 6n + 4.8 - \text{PAPR} \quad (68)$$

with  $n$  the number of quantization bits. For the standard 8-bit architecture of high-bandwidth ( $> 3$  GHz) digitizers, one obtains 52.8 dB minus the PAPR, to be compared with the DR and CDR values obtained before. A problem arises here with systems employing pulses, namely those based on direct or self-heterodyne detection: the PAPR of a typical transform-limited FSL pulse is of the order of the number of lines  $N$  and this results in traces prone to be limited by quantization noise. This calls for the use of correlation detection, either with digital or analog techniques. In digital pulse compression systems the SQNR does not constitute a limiting factor since, as already mentioned, quasi-CW FSL waveforms are available [12]. In dual combs, the availability of low-PAPR optical waveforms does not represent an advantage in the peak detection process, as these systems output a peaked, high-PAPR cross-correlation trace. However, the required detection

bandwidth of dual-comb systems is low (in the MHz range) and so the available number of quantization bits is much higher (typically  $> 12$ ). Hence, the SQNR does not represent a practical constraint in dual-comb correlation detection.

## V. DISCUSSION AND CONCLUSIONS

We have provided a theoretical framework to quantify the limitation of the SNR in FSL-based techniques set by the ASE of the amplifier. This study is valid for both acousto-optic and electro-optic FSLs. It is able to provide best-case performance values for FSL-based techniques. As expected, the obtained theoretical expressions are closely related to the type of receiver used in the system. As compared to heterodyne techniques (self-heterodyne and dual-comb), direct detection is penalized by the fact that the output voltage is proportional to the square modulus of the signal of interest. Additionally, the dual-comb technique shows the best SNR performance, owing to the compression factor of the detection bandwidth. A similar trend is reported in the two specific cases discussed here, coherent reflectometry and real-time Fourier transform, where dual-comb detection shows the best performance in terms of DR/CDR and sensitivity.

In the course of the analysis we have also pointed out a number of comparative advantages between the different receivers. In contrast to direct detection or to self-heterodyne receivers, which require transform-limited pulses, both digital and analog correlation receivers are more resilient to quantization noise and can be used with low-PAPR waveforms, hence amenable to high-power optical amplification if required. Also, digital pulse compression techniques attain a SNR similar to self-heterodyne detection of transform-limited pulses without the need of interferometer's stabilization.

In this study, we have assumed ideal optical components. In particular, we have supposed that the optical TBPF in the FSL has a perfect rectangular profile. In practice, the edges of the transmission function have a finite slope, which tends to increase ASE as compared to the ideal case depicted here. Additionally, the transmission window of a real bandpass filter is not strictly flat-top, which can alter the simple recurrence relations given in (2) and (5). The analytic treatment could be adapted to take into account the deviation of the TBPF transmission function from the ideal rectangular function.

Finally, our work raises the question on the reduction of the influence of ASE in FSL-based techniques. For this aim, several options can be considered. A first strategy consists of reducing the noise factor of the amplifier and increasing the transmission function of the FSL  $T$  by limiting as much as possible the losses of the optical components in the loop (TBPF, frequency shifter, fiber connectors). Another way of reducing ASE is to insert into the FSL a periodic bandpass filter, whose free spectral range matches precisely the frequency shift. It has been shown that the insertion of a multi-tap filter enables to clean the optical frequency comb at the output of electro-optic FSLs [11], [25], [44]. However, the extension of the technique to acousto-optic FSLs where the value of the frequency shift is much smaller (tens of MHz), seems challenging: it would require to lock the frequency of

the seed laser to a peak of the filter's transmission function. Moreover, spectral filtering in the FSL is not adapted to techniques like real-time Fourier transform, where the seed laser is modulated by a RF signal. Beside limiting ASE, the performance of FSL-based techniques can also be increased by temporal averaging. The gain in terms of performance can be computed depending on the type of receiver. From a practical perspective, averaging raises the question of the system's stability. Experimentally, FSL have been proven stable at the ms time scale [13], [33], while recently, stabilization schemes have been reported, enabling to maintain the coherence of the output up the hundreds of ms scale [16]. Of course, temporal averaging degrades the temporal response of the system, which can be inconvenient for real-time or dynamic applications.

#### APPENDIX A CORRELATIONS OF ASE SLICES

As is described by (4), the ASE field  $\epsilon(t)$  can be decomposed in ASE slices  $\alpha_n(t)$  with power  $a_n$  and constant spectrum of width  $f_s$ . Their statistical correlations are thus given by:

$$R_{\alpha_n}(u) = \langle \alpha_n(t)^* \alpha_n(t+u) \rangle = a_n \text{sinc}(f_s u) \quad (69)$$

where  $\text{sinc}(x) = \sin(\pi x)/\pi x$ . The statistical properties of the ASE field presented in Section II can be derived from the generalization of this formula to correlations of different slices. To this end, we introduce an alternative description based on the recurrence of the ASE generated in the FSL amplifier. Let us denote such a field by  $\epsilon_0(t)$ . In the rotating frame at frequency  $f_0$ , it can be decomposed in spectral slices as:

$$\epsilon_0(t) = \sum_{n=0}^{N-1} \eta_n(t) e^{i2\pi n f_s t} \quad (70)$$

Fields  $\eta_m(t)$  are zero-mean, mutually independent, circular gaussian stationary processes [41], centered at optical frequency  $f_0 + n f_s$ . Their ASE power is that contained in a spectral slice of width  $f_s$  and density  $n_{sp} h\nu(G-1)$ , so it coincides with  $a_0$  as defined in Section II:

$$\langle |\eta_m(t)|^2 \rangle = a_0 \quad (71)$$

In each recirculation, the initial ASE  $\epsilon_0(t)$  is first frequency shifted by  $f_s$  and then undergoes a delay by  $\tau_c$ . Then, it generates the ASE slices  $\alpha_n(t)$  according to:

$$\begin{aligned} \alpha_0(t) &= \eta_0(t) \\ \alpha_1(t) &= \eta_1(t) + \sqrt{GT} e^{-i\psi_1^0} \eta_0(t - \tau_c) \\ \alpha_2(t) &= \eta_2(t) + \sqrt{GT} e^{-i\psi_1^1} \eta_1(t - \tau_c) \\ &\quad + (\sqrt{GT})^2 e^{-i\psi_2^0} \eta_0(t - 2\tau_c) \end{aligned} \quad (72)$$

or, in general:

$$\alpha_n(t) = \sum_{k=0}^n (\sqrt{GT})^k e^{-i\psi_k^{n-k}} \eta_{n-k}(t - k\tau_c) \quad (73)$$

where  $\psi_k^m$  is the phase accumulated in  $k$  recirculations by a field initially centered at optical frequency  $f_0 + m f_s$ :

$$\psi_k^m = \pi f_s \tau_c k(k+1) + 2\pi k(f_0 + m f_s) \tau_c \quad (74)$$

The comb's spectral phases generated by the injected carrier are particular values corresponding to  $m = 0$ . Indeed,

$$\psi_k^0 = \pi f_s \tau_c k(k+1) + 2\pi k f_0 \tau_c = \phi_k + 2\pi k f_s \tau_c \quad (75)$$

recovering the phases of the spectral lines defined in (1). In general, these phases verify that  $\psi_k^m + \psi_q^{m+k} = \psi_{k+q}^m$ .

Expansion (73) indicates that  $\alpha_n(t)$  are circular gaussian processes and that the following recurrence in amplitude holds:

$$\alpha_n(t) = \eta_n(t) + \sqrt{GT} e^{-i\psi_1^{n-1}} \alpha_{n-1}(t - \tau_c) \quad (76)$$

This follows from (73) after noticing that  $\psi_k^{n-k} = \psi_{k-1}^{n-k} + \psi_1^{n-1}$ . Moreover,  $\langle \eta_n(t)^* \alpha_{n-1}(t - \tau_c) \rangle = 0$  since  $\alpha_{n-1}(t)$  does not contain  $\eta_n(t)$  in its expansion. Using this last observation we can prove the recurrence in power (5): if we multiply (76) side by side by its complex conjugate we get:

$$\begin{aligned} a_n &= \langle |\alpha_n(t)|^2 \rangle = \langle |\eta_n(t)|^2 \rangle + GT \langle |\alpha_{n-1}(t - \tau_c)|^2 \rangle \\ &= a_0 + GT \cdot a_{n-1} \end{aligned} \quad (77)$$

where we have also used (71).

To obtain the mutual correlation between ASE slices  $n+k$  and  $n$  with  $k > 0$ , we use (76) iteratively to find:

$$\begin{aligned} \alpha_{n+k}(t) &= \eta_{n+k}(t) + \sqrt{GT} e^{-i\psi_1^{n+k-1}} \eta_{n+k-1}(t - \tau_c) + \dots \\ &\quad + (\sqrt{GT})^{k-1} e^{-i\psi_{k-1}^{n+1}} \eta_{n+1}(t - (k-1)\tau_c) \\ &\quad + (\sqrt{GT})^k e^{-i\psi_k^n} \alpha_n(t - k\tau_c) \end{aligned} \quad (78)$$

Shifting the argument of this expression to  $t+u$ , multiplying it by  $\alpha_n(t)^*$ , and taking the statistical average we get:

$$\begin{aligned} \langle \alpha_n(t)^* \alpha_{n+k}(t+u) \rangle &= (\sqrt{GT})^k e^{-i\psi_k^n} R_{\alpha_n}(u - k\tau_c) \\ &= (\sqrt{GT})^k e^{-i\psi_k^n} a_n \text{sinc}(f_s u - k f_s \tau_c) \end{aligned} \quad (79)$$

where we have used again that  $\alpha_n(t)$  is independent of those  $\eta_m(t)$  with  $m > n$ . This shows that different ASE slices are mutually stationary and correlated only at multiples of the loop's round-trip time  $\tau_c$ , correlation that is responsible of the noise bumps at multiples of  $1/\tau_c$  found in the spectrum of the intensity fluctuations [35], [36].

The temporal extent of the correlation in (79) is  $\sim 1/f_s$ . This implies that, if  $f_s \tau_c \gg 1$ , the mutual correlation at equal times between different ASE slices,  $\langle \alpha_n(t)^* \alpha_{n+k}(t) \rangle$ , vanishes since in that case  $\text{sinc}(k f_s \tau_c) \simeq 0$  for  $k \neq 0$ . The required condition is met by practical implementations of FSL based on fiber loops where the product  $f_s \tau_c$  is typically 6 or higher. Without mutual correlation in amplitude at equal times, the recirculating ASE field behaves as an incoherent gaussian (or chaotic) optical field and (11) and (12) directly follow.

We end with the derivation of the ASE optical power spectral density, which will necessary in Appendix B. From (4), the cyclostationary correlation of the total ASE field is:

$$\begin{aligned} R_\epsilon(t, u) &= \langle \epsilon(t)^* \epsilon(t+u) \rangle \quad (80) \\ &= \sum_{n,m=0}^{N-1} \langle \alpha_n(t)^* \alpha_m(t+u) \rangle e^{i2\pi(m-n)f_s t} e^{i2\pi m f_s u} \end{aligned}$$

The optical spectral density is the Fourier transform of the temporal average in  $t$  of this correlation [42], [43]. This time-averaged correlation is denoted with an overline. The average selects only those terms in (80) with  $n = m$ , and so:

$$\overline{R_\epsilon}(u) = \overline{R_\epsilon(t, u)} = \sum_{n=0}^{N-1} a_n \text{sinc}(f_s u) e^{i2\pi n f_s u} \quad (81)$$

The optical spectral density is thus:

$$\mathcal{S}_\epsilon(f) = \sum_{n=0}^{N-1} \frac{a_n}{f_s} \text{rect}\left(\frac{f}{f_s} - n\right) \quad (82)$$

where the rectangle function is defined as  $\text{rect}(x) = 1$  for  $|x| < \frac{1}{2}$  and zero otherwise. The ASE spectral density is a stair of  $N$  steps with spectral density  $a_n/f_s$  and width  $f_s$ , in accordance with the power spectrum depicted in Fig. 2.

## APPENDIX B

### NOISE TERMS IN DUAL-COMB DETECTION

To compute the different rms noise values in dual-comb detection we first calculate the statistical correlation at full bandwidth (without low-pass filtering) of the corresponding noise terms. Then, we compute its spectral density by Fourier transform, and finally implement the low-pass filtering on the spectrum. The reference-ASE beat is  $v_{S'A}(t) = e'(t)\epsilon(t)^* + \text{cc}$  where cc denotes complex conjugation. Its correlation involves only two complex-conjugated terms, as those involving the product  $\langle \epsilon(t)\epsilon(t+u) \rangle$  or its complex conjugate are null due to the circularity of the ASE field. The correlation is:

$$\begin{aligned} \langle v_{S'A}(t)v_{S'A}(t+u) \rangle &= e'(t)e'(t+u)^* \langle \epsilon(t)^* \epsilon(t+u) \rangle + \text{cc} \\ &= R_\epsilon(t, u) \sum_{n,m=0}^{N-1} h_n h_m \sqrt{s'_n s'_m} e^{i2\pi(n-m)f'_s t} e^{-i2\pi m f'_s u} + \text{cc} \end{aligned} \quad (83)$$

The temporal average applies independently to correlation  $R_\epsilon(t, u)$  and  $e'(t)e'(t+u)^*$  since they have different periods  $1/f_s$  and  $1/f'_s$ , respectively. We get:

$$\overline{\langle v_{S'A}(t)v_{S'A}(t+u) \rangle} = \overline{R_\epsilon}(u) \sum_{n=0}^{N-1} h_n^2 s'_n e^{-i2\pi n f'_s u} + \text{cc} \quad (84)$$

and so its spectrum reads:

$$\mathcal{S}_{S'A}(f) = \sum_{n=0}^{N-1} h_n^2 s'_n [\mathcal{S}_\epsilon(f + n f'_s) + \mathcal{S}_\epsilon(-f + n f'_s)] \quad (85)$$

The noise spectral density consists of  $N$  frequency-shifted copies of the ASE spectrum weighted by the harmonics of the reference comb, together with its symmetric components. In terms of this spectrum, the (squared) rms noise value after low-pass filtering is:

$$\tilde{v}_{S'A}^2 = \int_{-B}^B df \mathcal{S}_{S'A}(f) \quad (86)$$

and so each frequency-shifted ASE spectrum  $\mathcal{S}_\epsilon(\pm f + n f'_s)$  only contributes at baseband with its  $n$ -th slice  $a_n/f_s$ :

$$\tilde{v}_{S'A}^2 = 2 \sum_{n=0}^{N-1} h_n^2 s'_n \times \frac{a_n}{f_s} \times 2B \quad (87)$$

This is the first of the equations in (50) after the exclusion of the  $n = 0$  term. The same type of analysis can be applied to the probe-ASE beat noise,  $v_{SA'}(t)$ , leading to the second of the equations in (50).

The final pair of noise terms represents the ASE-ASE beat,  $v_{AA'}(t) = \epsilon'(t)\epsilon(t)^* + \epsilon'^*(t)\epsilon(t)$ . The non-zero terms contributing to the statistical correlation are:

$$\begin{aligned} \langle \epsilon'(t)\epsilon(t)^* \epsilon'(t+u)^* \epsilon(t+u) + \epsilon'(t)^* \epsilon(t) \epsilon'(t+u) \epsilon(t+u)^* \rangle \\ = R_\epsilon(t, u) R_{\epsilon'}(t, u)^* + R_\epsilon(t, u)^* R_{\epsilon'}(t, u) \end{aligned} \quad (88)$$

Again, the time-averaged correlation is to be applied independently to  $R_\epsilon(t, u)$  and  $R_{\epsilon'}(t, u)$ . Performing the Fourier transform we get that the noise spectrum is expressed in terms of the cross-correlation of ASE spectra as:

$$\begin{aligned} \mathcal{S}_{AA'}(f) &= \int_{-\infty}^{+\infty} \mathcal{S}_\epsilon(f' + f) \mathcal{S}_{\epsilon'}(f') df' \\ &+ \int_{-\infty}^{+\infty} \mathcal{S}_\epsilon(f' - f) \mathcal{S}_{\epsilon'}(f') df' \end{aligned} \quad (89)$$

The ASE-ASE beat noise spectral density thus extends in bandwidth to the sum of the individual ASE spectra. Since the filtering is performed at baseband, the (squared) rms noise level can be approximated in terms of the dc value of  $\mathcal{S}_{AA'}(f)$  as  $\tilde{v}_{AA'}^2 = 2B \mathcal{S}_{AA'}(0) = 2B \times 2 \int \mathcal{S}_\epsilon(f') \mathcal{S}_{\epsilon'}(f') df'$ . The ASE spectra in (89) consist of  $N$  slices with respective densities of  $a_n/f_s$  and  $h_n^2 a'_n/f'_s$ , extending in widths  $f_s \simeq f'_s$ . Then we can approximate:

$$\mathcal{S}_{AA'}(0) \simeq 2 \sum_{n=0}^{N-1} \frac{a_n}{f_s} \times \frac{h_n^2 a'_n}{f'_s} \times f'_s \quad (90)$$

and this leads to (52).

## REFERENCES

- [1] G. Rajan, *Optical Fiber Sensors*, CRC Press, Taylor & Francis (2015).
- [2] T. Fujii, T. Fukuchi, *Laser Remote Sensing*, CRC Press, Taylor & Francis (2005).
- [3] J. Capmany, D. Novak, "Microwave photonics combines two worlds," *Nat. Photon.*, vol. 1, pp. 319–330, 2007.
- [4] V. J. Urick, K. J. Williams, and J. D. McKinney, *Fundamentals of Microwave Photonics*, John Wiley & Sons (2015).
- [5] T. Kawanishi, T. Sakamoto, S. Shinada, and M. Izutsu, "Optical frequency comb generator using optical fiber loops with single-sideband modulation," *IEICE Electron. Express*, vol. 1, no. 8, pp. 217–221, Jul. 2004.
- [6] J. Li, X. Li, X. Zhang, F. Tian, and L. Xi, "Analysis of the stability and optimizing operation of the single-side-band modulator based on re-circulating frequency shifter used for the T-bit/s optical communication transmission," *Opt. Express*, vol. 18, no. 17, pp. 17597–17609, Aug. 2010.
- [7] C. Lei, H. Chen, M. Chen, S. Yang and S. Xie, "Recirculating frequency shifting based wideband optical frequency comb generation by phase coherence control," *IEEE Photonics J.*, vol. 7, no. 1, pp. 1–7, Feb. 2015.
- [8] H. Guillet de Chatellus, L. Romero Cortés, and J. Azaña, "Arbitrary energy-preserving control of the line spacing of an optical frequency comb over six orders of magnitude through self-imaging," *Opt. Express*, vol. 26, no. 16, pp. 21069–21085, Aug. 2018.

- [9] V. Durán, H. Guillet de Chatellus, C. Schnébelin, K. Nithyanandan, J. Clement, and C. R. Fernández-Pousa, "Optical frequency combs generated by acousto-optic frequency-shifting loops," *IEEE Photon. Technol. Lett.*, vol. 31, no. 23, pp. 1878–1881, Dec. 2019.
- [10] F. Tian, X. Zhang, J. Li and L. Xi, "Generation of 50 stable frequency-locked optical carriers for Tb/s multicarrier optical transmission using a recirculating frequency shifter," *J. Lightw. Technol.*, vol. 29, no. 8, pp. 1085–1091, Apr. 2011.
- [11] J. Lin, L. Wang, M. Lyu, A. Pai, X. Zhang, S. LaRochelle, and L. A. Rusch, "Demonstration and evaluation of an optimized RFS comb for terabit flexible optical networks," *J. Opt. Commun. Netw.*, vol. 9, no. 9, pp. 739–746, Sep. 2017.
- [12] J. Clement, C. Schnébelin, H. Guillet de Chatellus and C. R. Fernández-Pousa, "Laser ranging using coherent pulse compression with frequency shifting loops," *Opt. Express*, vol. 27, no. 9, pp. 12000–12010, Apr. 2019.
- [13] V. Billault, V. Durán, C. R. Fernández-Pousa, V. Crozatier, D. Dolfi, and H. Guillet de Chatellus, "All-optical coherent pulse compression for dynamic laser ranging using an acousto-optic dual comb," *Opt. Express*, vol. 29, no. 14, pp. 21369–21385, Jul. 2021.
- [14] V. Durán, C. Schnébelin, and H. Guillet de Chatellus, "Coherent multi-heterodyne spectroscopy using acousto-optic frequency combs," *Opt. Express*, vol. 26, no. 11, pp. 13800–13809, May 2018.
- [15] H. Guillet de Chatellus, O. Jacquin, O. Hugon, W. Glastre, E. Lacot, and J. Marklof, "Generation of ultrahigh and tunable repetition rates in CW injection-seeded frequency-shifted feedback lasers," *Opt. Express*, vol. 21, no. 13, pp. 15065–15074, Jul. 2013.
- [16] V. Billault, V. Crozatier, G. Bailly, L. Morvan, D. Dolfi, N. Kanagaraj, and H. Guillet de Chatellus, "Phase noise of optical pulse trains generated by Talbot effect in frequency shifting loops," *J. Lightw. Technol.*, vol. 39, no. 8, pp. 2336–2347, Apr. 2021.
- [17] H. Guillet de Chatellus, L. Romero Cortés, and J. Azaña. "Optical real-time Fourier transformation with kilohertz resolutions," *Optica*, vol. 3, no. 1, pp. 1–8, Jan. 2016.
- [18] C. Schnébelin and H. Guillet de Chatellus, "Agile photonic fractional Fourier transformation of optical and RF signals," *Optica*, vol. 4, no. 8, pp. 907–910, Aug. 2017.
- [19] C. Pulikkaseril, E. H. W. Chan and R. A. Minasian, "Coherence-free microwave photonic bandpass filter using a frequency-shifting recirculating delay line," *J. Lightw. Technol.*, vol. 28, no. 3, pp. 262–269, Feb. 2010.
- [20] W. Dai, W. Rao, H. Wang and H. Fu, "Microwave photonic filter by using recirculating frequency shifter to generate optical frequency comb," *IEEE Photon. J.*, vol. 13, no. 2, pp. 1–8, Apr. 2021.
- [21] C. Schnébelin, L. R. Cortés, J. Azaña, H. Guillet de Chatellus, "Real-time measurement of complex fast signals by bandwidth compression in frequency shifting loops," *Opt. Lett.*, vol. 45, no. 6, pp. 1387–1390, Mar. 2020.
- [22] C. Schnébelin, J. Azaña, and H. Guillet de Chatellus, "Programmable broadband optical field spectral shaping with megahertz resolution using a simple frequency shifting loop," *Nat. Commun.*, vol. 10, Oct. 2019, Art. no. 4654.
- [23] K. Shimizu, T. Horiguchi, Y. Koyamada, and T. Kurashima, "Coherent self-heterodyne detection of spontaneously Brillouin-scattered light waves in a single-mode fiber," *Opt. Lett.*, vol. 18, no. 3, pp. 185–187, Feb. 1993.
- [24] Y. Liu, Z. Zhang, M. Burla, and B. J. Eggleton, "11-GHz-bandwidth photonic radar using MHz electronics," *Laser Photonics Rev.*, vol. 16, no. 4, Apr. 2002, Art. no. 2100549.
- [25] J. Lin, L. Xi, J. Li, X. Zhang, X. Zhang, and S. A. Niazi, "Low noise optical multi-carrier generation using optical-FIR filter for ASE noise suppression in re-circulating frequency shifter loop," *Opt. Express*, vol. 22, no. 7, pp. 7852–7864, Apr. 2014.
- [26] N. Kanagaraj, L. Djevarhidjian, V. Durán, C. Schnébelin, and H. Guillet de Chatellus, "Optimization of acousto-optic optical frequency combs," *Opt. Express*, vol. 27, no. 10, pp. 14842–14852, May 2019.
- [27] H. Tu, L. Xi, X. Zhang, X. Zhang, J. Lin, and W. Meng, "Analysis of the performance of optical frequency comb based on recirculating frequency shifter influenced by an Er-doped fiber amplifier," *Photon. Res.*, vol. 1, no. 2, pp. 88–91, Aug. 2013.
- [28] K. Shimizu, T. Horiguchi, and Y. Koyamada, "Frequency translation of light waves by propagation around an optical ring circuit containing a frequency shifter: I. Experiment," *Appl. Opt.*, vol. 32, no. 33, pp. 6718–6726, Nov. 1993.
- [29] K. Shimizu, T. Horiguchi, and Y. Koyamada, "Frequency translation of light waves by propagation around an optical ring circuit containing a frequency shifter: II. Theoretical analysis," *Appl. Opt.*, vol. 33, no. 15, pp. 3209–3219, May 1994.
- [30] K. Takano, K. Nakagawa, and H. Ito, "Influence of optical filters on pulse circulation in fiber rings with a frequency shifter and EDFAs," *Opt. Express*, vol. 14, no. 22, pp. 10313–10323, Oct. 2006.
- [31] L. P. Yatsenko, B. W. Shore, and K. Bergmann, "Theory of a frequency-shifted feedback laser," *Opt. Commun.*, vol. 236, no. 1–3, pp. 183–202, Jun. 2004.
- [32] H. Guillet de Chatellus, E. Lacot, W. Glastre, O. Jacquin, and O. Hugon, "Theory of Talbot lasers," *Phys. Rev. A*, vol. 88, no. 3, Sep. 2013, Art. no. 033828.
- [33] H. Guillet de Chatellus, L. Romero Cortés, C. Schnébelin, M. Burla, and J. Azaña, "Reconfigurable photonic generation of broadband chirped waveforms using a single CW laser and low-frequency electronics," *Nat. Commun.*, vol. 9, Jun. 2018, Art. no. 2438.
- [34] J. Clement, H. Guillet de Chatellus, and C. R. Fernández-Pousa, "Far-field Talbot waveforms generated by acousto-optic frequency shifting loops," *Opt. Express*, vol. 28, no. 9, pp. 12977–12997, Apr. 2020.
- [35] L. P. Yatsenko, B. W. Shore, and K. Bergmann, "Coherence in the output spectrum of frequency shifted feedback lasers," *Opt. Commun.*, vol. 282, no. 2, pp. 300–309, Jan. 2009.
- [36] H. Guillet de Chatellus and J.-P. Pique, "Statistical properties of frequency-shifted feedback lasers," *Opt. Commun.*, vol. 283, no. 1, pp. 71–77, Jan. 2010.
- [37] A. H. Hartog, *An Introduction to Distributed Optical Fibre Sensors*, CRC Press, Taylor & Francis (2017).
- [38] K. Shemer, G. Bashan, H. Hagai Diamandi, Y. London, T. Raanan, Y. Israelshvili, A. Charny, I. Cohen, A. Bergman, N. Levanon, and A. Zadok, "Sequence-coded coherent laser ranging with high detection sensitivity," *OSA Continuum*, vol. 3, no. 5, pp. 1274–1282, May 2020.
- [39] S. B. Alexander, *Optical Communication Receiver Design*, SPIE (1997).
- [40] I. Glover and P. Grant, *Digital Communications*, Prentice Hall (1998).
- [41] J. W. Goodman, *Statistical Optics*, John Wiley & Sons (2015).
- [42] A. Papoulis, *Probability, Random Variables, and Stochastic Processes*, 1st. ed., McGraw-Hill (1965).
- [43] W. A. Gardner, *Introduction to Random Processes*, McGraw-Hill (1989).
- [44] J. Li, J. Lin, X. Zhang, L. Xi, X. Tang, and Y. Qiao, "Scheme for generation of flat top and high signal-to-noise ratio optical frequency comb," *Chin. Opt. Lett.*, vol. 13, no. 1, Jan. 2015, Art. no. 010605.

**Carlos R. Fernández-Pousa** received the Ph.D. degree in physics from Universidad de Santiago de Compostela in 1998. In 1997 he moved to the Optics Division of Universidad Miguel Hernández de Elche, Spain, where he conducted research on optical recording materials, GRIN, diffractive and polarization optics. In 2004 he joined the Division of Signal Theory and Communications, Department of Communications Engineering, Universidad Miguel Hernández, where he is currently Full Professor and integrated in the Engineering Research Institute (I3E). His current topics of interest are optical coherence theory, microwave photonics systems, and fiber-based optical metrology. Dr. Hernández-Pousa is a Member of the Spanish Optical Society, Member of the Royal Spanish Society of Physics, Senior Member of the Photonics Society (IEEE), and Senior Member of Optica.

**Hugues Guillet de Chatellus** got his PhD in 2002 from the University of Bordeaux. His primary research topics were the use of ultrashort pulses to control and to characterize optical non linearities in glasses. Then, he spent two years as a postdoc at the Quantum Imaging Lab at Boston University, on the engineering of optical sources of entangled photons. After another postdoc position in biophotonics in Saint Etienne (France), he was hired by the French CNRS (Centre National de la Recherche Scientifique) in 2006 in Grenoble. He investigated the coherence properties of modelless lasers in order to use them for laser guide stars in astronomy. From 2013, he focused on the use of frequency shifting loops for various applications, including spectroscopy, metrology, remote sensing, and microwave photonics. In parallel, he investigated novel features of Talbot effect and self-imaging. In 2014–2015, he spent a sabbatical year in the group of José Azaña, in Montreal. In 2021, he was appointed research director at CNRS.